



Near East Desertification: impact of Dead Sea drying on convective rainfall

Samiro Khodayar^{1,2} and Johannes Hoerner¹

¹Institute of Meteorology and Climate Research (IMK-TRO), Karlsruhe Institute of
Technology (KIT), Karlsruhe, Germany

²Mediterranean Centre for Environmental Studies (CEAM), Valencia, Spain

Submitted to Atmospheric Chemistry and Physics

(HyMeX Inter-journal SI)

* Corresponding author. E-mail address: Khodayar_sam@gva.es (S. Khodayar)

Mediterranean Centre for Environmental Studies (CEAM),

Technological Park, Charles R. Darwin Street, 14 46980 - Paterna - Valencia - Spain



1 **Abstract**

2 The Dead Sea desertification-threatened region is affected by continual lake level decline
3 and occasional, but life-endangering flash-floods. Climate change has aggravated such
4 issues in the past decades. In this study, the impact of the Dead Sea drying on the severe
5 convection generating heavy precipitation in the region is investigated. Perturbation
6 simulations with the high-resolution convection-permitting regional climate model
7 COSMO-CLM and several numerical weather prediction (NWP) runs on an event time
8 scale are performed over the Dead Sea area. A reference simulation covering the 2003
9 to 2013 period and a twin sensitivity experiment, in which the Dead Sea is dried out and
10 set to bare soil, are compared. NWP simulations focus on heavy precipitation events
11 exhibiting relevant differences between the reference and the sensitivity decadal
12 realization to assess the impact on the underlying convection-related processes.

13 On a decadal scale, the difference between the simulations points out that in future
14 regional climate, under ongoing lake level decline, a decrease in evaporation, higher air
15 temperatures and less precipitation is to expect. Particularly, an increase in the number
16 of dry days and in the intensity of heavy precipitation is foreseen. The drying of the Dead
17 Sea is seen to affect the atmospheric conditions leading to convection in two ways: (a)
18 the local decrease in evaporation reduces moisture availability in the lower boundary
19 layer locally and in the neighbouring, directly affecting atmospheric stability. Weaker
20 updrafts characterize the drier and more stable atmosphere of the simulations where the
21 Dead Sea has been dried out. (b) Thermally driven wind system circulations and resulting
22 divergence/convergence fields are altered preventing in many occasions convection
23 initiation because of the omission of convergence lines.

24

25

26

27

28

29

30 *Key Words: Dead Sea drying, climate change, convection, heavy precipitation,*
31 *boundary layer, wind systems, high-resolution modelling*



32 1. Introduction

33 The Eastern Mediterranean and the Middle East is a sensitive climate change area
34 (Smiatek et al. 2011). The anticipated warming in the 21st century combined with the
35 general drying tendency, suggest important regional impacts of climate change, which
36 should be investigated to assess and mitigate local effects on society and ecosystems.
37 The Dead Sea basin, dominated by semi-arid and arid climates except by the north-
38 western part that is governed by Mediterranean climate (Greenbaum et al. 2006), is an
39 ideal area to study climate variation in the Near East. It was already discussed by Ashbel
40 (1939) the influence of the Dead Sea on the climate of its neighbouring regions. The
41 change in the climate of the Dead Sea basin caused by the drying of the Dead Sea has
42 also been evidenced in the last decades (Alpert et al. 1997; Cohen and Stanhill 1996;
43 Stanhill 1994). The Dead Sea is the lowest body of water in the world (~ -430 m)
44 surrounded by the Judean Mountains (up to ~ 1 km amsl) to the west and to the east by
45 the Maob Mountains (up to ~ 3 km amsl). The area in between is rocky desert. The
46 complex topography of the area favours the combined occurrence of several wind
47 regimes in addition to the general synoptic systems, namely valley and slope winds,
48 Mediterranean breezes and local lake breezes (e.g. Shafir and Alpert 2011). These wind
49 systems are of great importance for the living conditions in the region since they influence
50 the visibility and the air quality (e.g. Kalthoff et al. 2000; Corsmeier et al. 2005) as well
51 as the atmospheric temperature and humidity. Since the Dead Sea is a terminal lake of
52 the Dead Sea Valley, no natural outflow exists, being evaporation the main loss of water
53 (Metzger et al. 2017). Through the high evaporation the lake level declines and results
54 in a desertification of the shoreline and a changing fraction of water and land surface in
55 the valley. The documented Dead Sea water level drop of about 1 m/y in the last decades
56 (Gavrieli et al. 2005) severely affects agriculture, industry and the environmental
57 conditions in the area, thus, leading to substantial economic losses (Arkin and Gilat
58 2000).

59 The Jordan River catchment and Dead Sea-exhibit in the north, annual precipitation in
60 the order of 600-800 mm, whereas in the south, there is an all year arid climate with an
61 annual precipitation of <150 mm (Schaedler and Sasse 2006). Rain occurs between
62 October and May and can be localized or widespread (Dayan and Sharon 1980) with
63 annual variations of the same order of magnitude as the rainfall itself (Sharon and Kutiel
64 1986). Rainfall varies seasonally and annually, and it is often concentrated in intense
65 showers (Greenbaum et al. 2006). The Dead Sea basin is prone to flash flooding caused
66 mainly by severe convection generating heavy precipitation (Dayan and Morin 2006).
67 Flash floods are among the most dangerous meteorological hazards affecting the



68 Mediterranean countries (Llasat et al 2010), thus, knowledge about the processes
69 shaping these events is of high value. This is particularly relevant in arid climates, where
70 rainfall is scarce, and often, local and highly variable. In flood-producing rainstorms,
71 atmospheric processes often act in concert at several scales. Synoptic-scale processes
72 transport and redistribute the excess sensible and latent heat accumulated over the
73 region and subsynoptic scale processes determine initiation of severe convection and
74 the resulting spatio-temporal rainfall characteristics. The main responsible synoptic
75 weather patterns leading to heavy rainfall in the region are in general well known and
76 described in previous publications (e.g. Belachsen et al. 2017; Dayan and Morin 2006).
77 Belachsen et al. (2017) pointed out that three main synoptic patterns are associated to
78 these rain events: Cyprus low accounting for 30% of the events, Low to the east of the
79 study region for 44%, and Active Red Sea Trough for 26%. The first two originate from
80 the Mediterranean Sea, while the third is an extension of the Africa monsoon. Houze
81 (2012) showed that orographic effects lead to enhanced rainfall generation; rain cells are
82 larger where topography is higher. Sub-synoptic scale processes play a decisive role in
83 deep convection generation in the region. Convection generated by static instability
84 seems to play a more important role than synoptic-scale vertical motions (Dayan and
85 Morin 2006). The moisture for developing intensive convection over the Dead Sea region
86 can be originated from the adjacent Mediterranean Sea (Alpert und Shay-EL 1994) and
87 from distant upwind sources (Dayan and Morin 2006).

88 In this study, the climatic change at the Dead Sea region caused by its drying is
89 investigated focusing on the impact on atmospheric conditions leading to heavy
90 precipitating convection in the region. The relevance of the Dead Sea as a local source
91 of moisture for precipitating convection as well as the impact of the energy balance
92 partitioning changes and related processes caused by the drying of the Dead Sea are
93 investigated. With this purpose, a sensitivity experiment with the high-resolution regional
94 climate model COSMO-CLM [Consortium for Small scale Modelling model (COSMO)-in
95 Climate Mode (CLM); Böhm et al. 2006] is conducted. The high horizontal grid spacing
96 used (~ 2.8 km) resolves relevant orographic and small-scale features of the Dead Sea
97 basin, which is not the case when coarser resolution simulations are performed.
98 Moreover, at this resolution convection is explicitly resolved instead of being
99 parametrized, which has been already extensively demonstrated to be highly beneficial
100 for the simulation of heavy precipitation and convection-related processes (e.g., Prein et
101 al., 2013; Fosser et al., 2014; Ban et al., 2014). This effort, to the knowledge of the
102 authors, has not been previously attempted in the region.



1103 The impact of completely drying the Dead Sea on the regional atmospheric conditions
1104 and precipitating convection is discussed. A decadal simulation and several event-based
1105 Numerical Weather Prediction (NWP) runs covering the eastern Mediterranean are
1106 carried out. A process understanding methodology is applied to improve our knowledge
1107 about how sub-synoptic scale processes leading to severe convection are affected by
1108 the drying of the Dead Sea. The article is organized as follows. Section 2 provides an
1109 overview of the data and the methodology used. Then, in section 3, the climatology of
1110 the region based on the high-resolution convection-permitting decadal simulation is
1111 presented and the impact of drying the Dead Sea is examined across scales. Finally,
1112 conclusions are discussed in section 4.

1113

1114 **2. Data and methodology**

1115 **2.1 The COSMO-CLM model**

1116 In this investigation, the regional climate model (RCM) of the non-hydrostatic COSMO
1117 model, COSMO-CLM, is used (Version 5.0.1). It has been developed by the Consortium
1118 for Small-scale modeling (COSMO) and the Climate Limited-area Modeling Community
1119 (CLM) (Böhm et al., 2006). It uses a rotated geographical grid and a terrain-following
1120 vertical coordinate. The model domain covers the southern half of the Levant, centered
1121 around the Dead Sea, with a horizontal resolution of 7 km and 2.8 km, 60 vertical levels
1122 and a time step of 60 and 20 seconds, respectively. The driving data for the 7 km with a
1123 horizontal resolution of 0.25° is derived from the IFS (Integrated Forecasting System)
1124 analysis, the spectral weather model of ECMWF (European Centre for Medium-Range
1125 Weather Forecast). Additionally, orography data from GLOBE (Global Land One-km
1126 Base Elevation Project) of NOAA (National Oceanic and Atmospheric Administration)
1127 and soil data from HWSD (Harmonized Worlds Soil Database) TERRA is used. HWSD
1128 is a global harmonization of multiple regional soil data sets with a spatial resolution of
1129 0.008° (FAO, 2009), resulting in 9 different soil types in the model, namely 'ice and
1130 glacier', 'rock / lithosols', 'sand', 'sandy loam', 'loam', 'loamy clay', 'clay', 'histosols', and
1131 'water'.

1132 With a horizontal resolution below 3 km, convection can be resolved directly (Doms and
1133 Baldauf, 2015). The model physics includes a cloud physics parameterization with 5
1134 types of hydrometeors (water vapor, cloud water, precipitation water, cloud ice,
1135 precipitation ice), a radiative transfer scheme based on a delta-two-stream solution



136 (Doms et al., 2011) and a roughness-length dependent surface flux formulation based
137 on modified Businger relations (Businger et al., 1971).

138 Multiple model runs have been performed. A 7 km run from 2003 to 2013 with daily output
139 is used as nesting for two 2.8 km runs over the same time span. The Dead Sea is dried
140 out and replaced with soil types from the surrounding area in one of them (SEN), the
141 other one is used as reference (CLIM). For the detailed investigation of convective events
142 on 14.11.2011 and 19.11.2011, sub-seasonal simulations have been performed with the
143 same settings as the decadal simulation, but with hourly outputs.

144 **2.2 Methodology**

145 In order to assess the impact of the drying of the Dead Sea on the atmospheric conditions
146 leading to severe convection in the region, a set of sensitivity experiments was
147 performed. A decadal simulation covering the 2003 to 2013 time period was carried out
148 with the convection permitting 2.8 km COSMO-CLM model. Lateral boundary conditions
149 and initial conditions are derived from the European Centre for Medium-Range Weather
150 Forecasts (ECMWF) reanalysis data. The COSMO-CLM 7 km is used as nesting step in
151 between the forcing data and the 2.8 km run. This reference simulation will be hereafter
152 referred to as REF^{CLIM} simulation. Parallel to this, a sensitivity experiment (hereafter
153 SEN^{CLIM}) is carried out in which the Dead Sea is dried out and set to bare soil on -405 m
154 level (depth of the Dead Sea in the external data set, GLOBE (Hastings and Dunbar,
155 1999)). After examination of the results, the first year of simulations is considered spin-
156 up time, thus, our analysis covers the 2004-2013 period.

157 Regional dry and wet periods are identified and quantified in the simulations by means
158 of the Effective Drought Index (EDI; Byun and Wilhite 1999; Byun and Kim 2010). The
159 EDI is an intensive measure that considers daily water accumulations with a weighting
160 function for time passage normalizing accumulated precipitation. The values are
161 accumulated at different time scales and converted to standard deviations with respect
162 to the average values. Here we use an accumulation period of 365 days. EDI dry and
163 wet periods are categorized as follows: moderate dry periods $-1.5 < \text{EDI} < -1$, severe dry
164 periods $-2 < \text{EDI} < -1.5$, and extreme dry periods $\text{EDI} < -2$. Normal periods are revealed by
165 $-1 < \text{EDI} < 1$ values.

166 Based on daily mean values, precipitation and evapotranspiration distribution and
167 possible trends in the 10-year period are assessed. The study area is divided in four
168 subdomains centred at the Dead Sea to examine dependencies in relation to the regional
169 patterns (Figure 1). Differences in the annual cycle and temporal evolution of



170 precipitation and evapotranspiration between the REF^{CLIM} and SEN^{CLIM} are discussed.
171 Also, differences in the near-surface and boundary layer conditions and geopotential
172 height patterns are examined. Geographical patterns of mean evapotranspiration and
173 precipitation and differences with respect to the reference simulation are assessed.
174 Probability distribution functions (PDFs), and the Structure, Amplitude and Location
175 (SAL: Wernli et al. 2008) analysis methodologies are used to illustrate differences in the
176 mean and extreme precipitation between the reference and the sensitivity experiments.
177 The SAL is an object-based rainfall verification method. This index provides a quality
178 measure for the verification of quantitative precipitation forecasts considering three
179 relevant aspects of precipitation pattern: the structure (S), the amplitude (A), and the
180 location (L). The A component measures the relative deviation of the domain-averaged
181 rainfall; positive values indicate an overestimation of total precipitation, negative values
182 an underestimation. The component L provides an estimation of the 'accuracy of
183 location', comparing the proportion of high and low rainfall totals within each object. The
184 component S is constructed in such a way that positive values occur if precipitation
185 objects are too large and/or too flat and negative values if the objects are too small and/or
186 too peaked, quantifying the physical distance between the centres of mass of the two
187 rainfall fields to be compared. Perfect agreement between prediction and reference are
188 characterized by zero values for all components of SAL. Values for the amplitude and
189 structure are in the range $(-2, 2)$, where ± 0.66 represents a factor of 2 error. The location
190 component ranges from 0 to 2, where larger values indicate a greater separation
191 between centres of mass of the two rainfall fields. This is done by selecting a threshold
192 value of 1/15 of the maximum rainfall accumulation in the domain (following Wernli et al.
193 2008). The structure and location components are thus independent of the total rainfall
194 in the domain.

195

196 Differences in the temporal evolution of precipitation between the REF^{CLIM} and SEN^{CLIM}
197 are identified. Those events in which an area-mean (study area, Figure 1) difference
198 between both simulations higher than ± 0.1 mm/d exists are classified attending to their
199 synoptic scale environment, and atmospheric stability conditions.

200 Although Dayan and Morin (2006) discuss that in general large-scale vertical motions do
201 not provide the sufficient lifting necessary to initiate convection, it was demonstrated by
202 Dayan and Sharon (1980) that a relationship exists between the synoptic-scale weather
203 systems and deep moist convection, being those systems responsible for the
204 moisturizing and destabilization of the atmosphere prior to convective initiation. They
205 pointed out that indices of instability proved the most efficient determinants of the



206 environment characterizing each rainfall type in the region. Thus, two indicators of the
207 atmospheric degree of stability/instability, namely the Convective Available Potential
208 Energy (CAPE; Moncrieff and Miller 1976) and the KO-index (Andersson et al. 1989),
209 are examined in this study. The CAPE is a widely known index indicating the degree of
210 conditional instability. Whereas, the KO-index, which is estimated based on the
211 equivalent potential temperature at 500, 700, 850 and 1000 hPa (following the
212 recommendations by Bolton 1980), describes the potential of deep convection to occur
213 as a consequence of large-scale forcing (Andersson et al. 1989; Khodayar et al. 2013).
214 Generally, regions with KO-index < 2 K and large-scale lifting are identified as favourable
215 for deep convection. Parcel theory (50 hPa ML (Mixed Layer) parcel) and virtual
216 temperature correction (Doswell and Rasmussen 1994) are applied to these
217 calculations.

218 Based on the above criteria, a separation was made between events with widespread
219 rainfall and those more localized. Among the latter, we selected two events to illustrate
220 the local impacts on the boundary layer conducive to deep moist convection. Particularly,
221 differences in the amount, structure and location of precipitation are assessed by
222 examining the spatial patterns and the SAL verification method. High-resolution
223 simulations with the NWP COSMO 2.8 km model are performed with hourly output
224 temporal resolution and covering a 3-day period (including 48-h prior to the day of the
225 event, from 00 UTC) to capture atmospheric pre-conditions conducive to deep moist
226 convection. For this, a reference simulation, REF^{NWP}, and a sensitivity experiment,
227 SEN^{NWP}, are carried out for each event.

228

229 **3. Results and discussion**

230 **3.1 Climatology of the Dead Sea region**

231 *Annual cycle*

232 To assess the climatology of the study region (Figure 1) the annual evaporation and
233 precipitation cycles based on daily means of the respective quantities are investigated
234 (Figure 2). Additionally, we examine the evolution of specific humidity (Q_{v2m}) and
235 temperature at 2 m (T_{2m}) as well as total column integrated water vapour (IWV) and low-
236 boundary layer (< 900 hPa) equivalent potential temperature (Θ_e). Possible changes in
237 the atmospheric stability conditions are evaluated by examination of the CAPE and KO-
238 index. In Figure 2, all grid points over the study region (Figure 1) and the time period



239 2004-2013 are considered. Differences between the REF^{CLIM} and the SEN^{CLIM}
240 simulations are also discussed.

241 The annual cycle of evaporation shows minimum values in the autumn season (around
242 October, ~ 0.1 mm/d) and maximum evaporation in spring (around March, ~ 0.4 mm/d).
243 The dependency with the precipitation cycle is clear with maximum values of the latter
244 around March and rain occurring between October and May (Figure 2a) in agreement
245 with observations in the area (Dayan and Sharon 1980). The difference between the
246 evaporation in the REF^{CLIM} and the SEN^{CLIM} simulations indicates a mean decrease in
247 the order of 0.02 (February) to ~ 0.1 (August) mm/d in the absence of the Dead Sea
248 water (SEN^{CLIM}). The largest difference is in the dry period (May to October) when water
249 availability is less dependent on precipitation, and evaporation is higher over the Dead
250 Sea in contrast to the minimum values over land (Metzger et al. 2017). In general, there
251 is a decrease of about 0.5 % in precipitation in the “non-Sea” simulation, SEN^{CLIM}. In
252 contrast to the differences in evaporation, precipitation differences between the
253 reference and the sensitivity experiment occur in both directions during the rain period,
254 from October to May. Examining the total number over the whole decadal simulation it is
255 seen that the number of dry or wet days (> 0.1 mm/d) or heavy precipitation events is
256 not largely affected in the sensitivity experiment. In general, the number of dry days
257 increases (fewer wet days) in the SEN^{CLIM} simulation, whereas the number of high
258 intensity events show almost no variation. For each simulation, the difference between
259 precipitation and evaporation is negative mainly in spring and summer contributing to the
260 dryness in the region. Furthermore, the negative difference between the REF^{CLIM} and
261 SEN^{CLIM} simulations indicates that the PREC-EVAP difference is higher in the SEN^{CLIM}
262 simulation probably in relation to the reduced evaporation over the dry sea area and the
263 general decrease in the precipitation amount in the region.

264 In addition to the reduced evaporation and precipitation in the whole domain in the
265 SEN^{CLIM} simulation a drier and warmer lower-troposphere is identified (Figure 2b) in
266 agreement with the observational assessment by Metzger et al. (2017) of the cooling
267 effect of evaporation on air temperature in the region. The annual cycle of IWW and
268 $\Theta_{e<900hPa}$ in Figure 2c show that the impact of the dry Dead Sea resulting evaporation is
269 less pronounced when a deeper atmospheric layer is considered. Indeed, $\Theta_{e<900hPa}$
270 evolution evidences that the warming effect due to the decreased evaporation in the
271 SEN^{CLIM} simulation is restricted to the near surface.

272 In Figure 2d, the annual cycle of areal mean CAPE displays larger values in the period
273 from August to November, being this the period more favourable for convection. Positive



274 CAPE differences between the REF^{CLIM} and the SEN^{CLIM} simulations are presumably in
275 relation to the identified distinct lower-atmospheric conditions, being these more
276 favourable and consequently CAPE values higher in the REF^{CLIM} simulation. In the same
277 period, the KO-index indicates a more potentially unstable atmosphere, i.e. prone to
278 deep convection because of large-scale forcing, and larger differences between
279 simulations.

280 To further assess the most affected areas in our investigation domain, the study region
281 is divided in four subdomains surrounding the Dead Sea (Figure 3). Annual cycles are
282 separately investigated to take into consideration the relevant differences in orography,
283 soil types, and distance to the coast among others (Figure1), which are known to have
284 a significant impact in the precipitation distribution in the region (e.g. Belachsen 2017;
285 Houze 2012). In agreement with the well-known precipitation distribution in the region
286 most of the events occur in A1 (north-east) and A2 (north-east). Also, in these
287 subdomains larger differences between the REF^{CLIM} and SEN^{CLIM} simulations are
288 identified pointing out the relevance of the Dead Sea evaporation in the pre-convective
289 environment for rainfall episodes over the study area (Figure3a). Considering only land
290 grid points almost no difference between simulations is found in the evaporation annual
291 cycle of A1 and A2 (Figure3b) suggesting the distinct amount of moisture advected
292 towards A1 and A2 from the Dead Sea in REF^{CLIM} and SEN^{CLIM} as responsible for the
293 differences in the boundary layer conditions conducive to convection. Also, in these
294 subdomains the dryer and warmer lower boundary layer and the reduced instability in
295 the SEN^{CLIM} are recognized

296 *Inter-annual variability*

297 In Figures 4 we discuss the inter-annual variability (based on monthly-daily areal mean
298 values) of evaporation, precipitation as well as drought evolution.

299 The reduced evaporation in the annual cycle of the SEN^{CLIM} simulation for the whole
300 investigation domain, resulting from the drying of the Dead Sea and affected evaporation,
301 remains from year to year (Figure 4a). Larger differences between the simulations occur
302 in the May to November months in agreement with the annual cycle in Figure 2a. This,
303 and the time period of the maximum/minimum is constant over the years. A tendency
304 towards lower evaporation at each simulation and higher differences between both at
305 the end of the period are identified. An inter-annual fluctuation is observed in both
306 REF^{CLIM} and SEN^{CLIM} simulations. The yearly rate of evaporation shows, for example, in
307 REF^{CLIM} maximum values of about 7 mm in 2011 and around 17 mm in 2012. This is in
308 agreement with the positive correlation expected between precipitation and evaporation,



309 a trend towards decreased precipitation and a correspondence between drier years such
310 as the 2011-2012 period and lower annual evaporation are seen in Figure 4b. Year to
311 year EDI calculations in Figure 4c help us identify the regional extreme dry and wet
312 periods. The EDI range of variation from about -1 to 2 for the whole period of simulation
313 indicates that the dry condition is the common environment in the area, while the wet
314 periods, EDI up to 6, could be identified as extreme wet periods (relative to the area), in
315 this case in the form of heavy precipitation events. Maximum positive EDI values are in
316 the first months of the year in agreement with the precipitation annual cycle in Figure 2,
317 whereas minimal EDI values occur in summer and autumn indicative of the dry conditions
318 in these periods. Differences in the EDI calculations from both simulations reveal distinct
319 precipitation evolutions and denote timing differences in the occurrence of the
320 precipitation events. When the regional climate evolution is examined in combination
321 with the impact on the number of heavy precipitation events (Table 1) the impact is
322 stronger in the dry period of 2011 (Figure 4a). About six events show relevant differences
323 in this period, contrary to the average 3 episodes per year.

324 *Spatial distribution*

325 The geographical patterns of evaporation and precipitation are presented in Figure 5.
326 Over the Dead Sea, the simulated average annual evaporation for the period under
327 consideration is in the order of 1500-1800 mm/y, in contrast to the values in the deserts
328 east and south, where the evaporation is less than 20 mm/y. Observed annual
329 evaporation of this lake is known to be about 1500 mm and to vary with the salinity at
330 the surface of the lake and freshening by the water inflow (Dayan and Morin 2006). Over
331 land, higher evaporation is seen over the Judean Mountains and the Jordanian
332 Highlands. High correlation with the orography and soil types is seen (Figure 1).
333 Particularly, in the Jordanian Highlands where maximum evaporation is around 200
334 mm/y, the complex topography coincides with sandy loam soils, whereas most of the soil
335 in study region is defined as loamy clay or clay (Figure 1). The evaporative difference
336 field between simulations in Figure 5a shows a highly inhomogeneous patchiness not
337 evidencing any relationship with orography or soil type, but rather with changes in the
338 precipitation pattern in the SEN^{CLIM} simulation as seen in Figure 5b.

339 In agreement with the temporal series of areal mean precipitation in Figure 3 higher
340 annual precipitation are in the north-west and -east, with respect to the southern regions.
341 Topographic features exert a large impact on precipitation distribution with maxima of
342 about 175 to 300 mm/y over the Judean Mountains and the Jordanian Highlands. To the
343 northern end of the Dead Sea valley, the largest precipitation difference between the



344 REF^{CLIM} and the SEN^{CLIM} simulations is identified, rather than directly over the Dead Sea
345 area noting the importance of advected moisture from the Dead Sea evaporative flux
346 upslope and along the Dead Sea valley as well as the indirect effects of a different spatial
347 distribution of low-tropospheric water vapour in the occurrence of precipitating
348 convection.

349 Regarding the impact on the large-scale conditions, differences in the spatial pattern and
350 strength of the 500 hPa geopotential height field are identified over the Dead Sea (not
351 shown). In the 10-year mean, differences up to 0.002gpdm higher in SEN than in REF
352 are observed. Around the Dead Sea area, the differences are smaller and more irregular.
353 Generally, the differences are higher in the east of the Dead Sea than in the west.

354

355 *Precipitation probability distribution function*

356 While the probability for lower intensity precipitation is very similar in the REF^{CLIM} and the
357 SEN^{CLIM} simulations differences are recognized in the higher precipitation intensities,
358 from about 150 mm/d (Figure 6a). Particularly, above 180 mm/d extreme precipitation
359 values occur less frequent at the SEN^{CLIM} simulation where a drier, warmer and more
360 stable atmosphere is identified (Figure 2).

361 *SAL*

362 The use of the SAL method in this study differs from the approach frequently presented
363 in literature since it is here not our purpose to examine differences between the simulated
364 field and observations (adequate observations for this comparison are not available in
365 the area), but to compare changes regarding the structure, amount and location of the
366 precipitation field between our reference and sensitivity experiments. Figure 6b shows
367 that when the mean precipitation over the whole simulation period is considered all three
368 SAL components are close to zero 0, meaning that very small differences are found.
369 However, when single precipitation events in the REF^{CLIM} simulation are compared with
370 the same period at the SEN^{CLIM} simulation, larger differences regarding structure,
371 amount and location of rainfall events are found. For further examination of this issue
372 two exemplary heavy precipitation events (indicated by boxes in Figure 6b) are analysed
373 in detail. In both cases, a negative A-component is recognized, that is, less precipitation
374 falls in the SEN^{CLIM} simulation. The S-component also evidences the change in the
375 structure of the convective cells. The L-component is low meaning that the convective
376 location does not change significantly in the SEN^{CLIM} simulation, in contrast to the
377 intensity and structure of the cells.



378

379 **3.2 Sensitivity of atmospheric conditions to the Dead Sea drying: episodic**
380 **investigation**

381 Among those events exhibiting differences in the precipitation field between both
382 simulations (Table 1 and Figure 6b) two situations occurring in the time period of the 14
383 to 19 November 2011 are investigated in the following.

384 In this term, the synoptic situation is characterized by a Cyprus low and its frontal system
385 located over the Dead Sea at about 00 UTC on the 15 November 2011 and at 12 UTC
386 on the 18 November 2011. The low-pressure system and its frontal system induced
387 strong south-westerly to westerly winds with mean wind velocities up to 15 m/s.

388 In the first situation (hereafter CASE1), in association with the western movement of the
389 cold front a convective system develops over the Jordanian Highlands with precipitation
390 starting at about 21 UTC on the 14 November 2011. This convective system is of high
391 interest because of the large difference in its development between the REF^{14.11} and the
392 SEN^{14.11} simulations.

393 In Figure 7a the 24-h accumulated precipitation, from 14.11 09 UTC to 15.11 08 UTC, in
394 the investigation area is shown for the REF^{14.11} and the SEN^{14.11} simulations. Two
395 precipitation areas are seen, on the north-western and north-eastern of the Dead Sea.
396 Larger difference between models is on the north-eastern region (24-h accumulated
397 precipitation > 100 mm/d in REF^{14.11}, while < 50 mm/d in SEN^{14.11}), which is the focus of
398 our analysis.

399

400 The REF^{14.11} simulation shows that in the 6 hours period prior to the initiation of
401 convection the pre-convective atmosphere and more specifically the lower boundary
402 layer exhibit a moist (IWV ~ 24-30 mm, qvPBLmax ~ 7-10 g/kg) and unstable (CAPE ~
403 1100 J/kg; KO-index ~ -8 K; not shown) air mass on the western side of the investigation
404 area, particularly close to the western Mediterranean coast, and drier (IWV~ 8-16;
405 qvPBLmax ~ 4-6 g/kg) and more stable conditions (CAPE < 200 J/kg; KO-index ~ 0-2 K)
406 on the eastern side of the domain (Figure 7b). A maximum gradient of about 5 g/kg from
407 west to east is established in the lower boundary layer.

408 Main differences between both simulations are over the Dead Sea (IWV difference up to
409 2 mm and qvPBL up to 1.5 g/kg) and north and north-east of it, but almost similar
410 conditions everywhere else. In our target area (subdomain of investigation where the



411 convection episode takes place (red box in Figure 7)), north-east of the Dead Sea, a
412 drier and a more stable atmosphere is identified at the SEN^{14,11} simulation.

413 The evolution of the wind circulation systems in the area is similar in both simulations
414 (Figure 7c). The 700 hPa, 850 and 950 hPa winds dominantly blow from the south south-
415 west during the pre-convective environment advecting the moist unstable air mass
416 towards the Dead Sea valley and north-east of it, directly affecting the atmospheric
417 conditions at the target area. In both simulations, the passage of the cold front over the
418 Dead Sea establishes a strong southerly wind from about 10 UTC on the 14 November
419 2011.

420 Prior to this time, dry air was advected below about 850 hPa towards the target area
421 from the east. The turning of the low-level winds and the resulting moistening of the
422 atmosphere is well and equally captured by both simulations (Figure 8a). Furthermore,
423 at the near-surface, from about 16 UTC, ~ 5 h prior to convection initiation in the target
424 area, a near-surface convergence line forms at the foothills of the northern part of the
425 Jordanian Highlands, which is also well and equally captured by both simulations (Figure
426 8b). The lifting provided by the convergence line triggers convection in the area.
427 However, the drier and more stable atmosphere in the SEN^{14,11}simulation results in less
428 intense convection, weaker updrafts, and reduced precipitation at the eastern slope of
429 the valley.

430

431 In the second case, CASE2, we address an episode of localized convection taking place
432 on the north-western edge of the Dead Sea in the REF simulation, whereas no
433 convection develops in the SEN simulation. The isolated convection in the REF
434 simulation left about 50 mm rain in 3 h starting at about 03 UTC on the 19 November
435 2011 (Figure 9).

436 In contrast to CASE1, the modification of the pre-convective environment relevant for
437 convective initiation is in this case dominated by dynamical changes in the mesoscale
438 circulations. Differences in the evolution and strength of the Mediterranean Sea Breeze
439 (MSB), the Dead Sea breeze and orographic winds influence atmospheric conditions in
440 the target area leading to the assistance to or to the absence of convection. The most
441 significant difference observed between the simulations is in the development of a strong
442 near-surface convergence line in the REF simulation (which is not present in the SEN
443 simulation hindering convection in the area), which forms about 2 h before convective
444 initiation (Figure 10).



445 Even in the first hours of the 18 November 2011 differences in the speed and direction
446 of the near-surface winds over the Dead Sea and on the eastern flank of the Jordanian
447 Highlands could be identified. A fundamental difference between simulations occurs from
448 about 17 UTC when strong westerly winds indicating the arrival of the MSB reach the
449 western shore of the Dead Sea. One hour later, in the REF^{19,11} run the MSB strongly
450 penetrates the Dead Sea valley reaching as far as the eastern coast in the centre to
451 south areas. However, in the SEN^{19,11} simulation the MSB does not penetrate downward,
452 instead strong northerly winds flow along the valley (Figure 10a). Numerous
453 observational and numerical studies carried out to investigate the dynamics of the MSB
454 (e.g. Naor et al. 2017; Vuellers et al. 2018) showed that the downward penetration of the
455 MSB results from temperature differences between the valley air mass, which is warmer
456 than the maritime air mass. An examination of temperature differences along a near-
457 surface north-south valley transect (positions in Figure 10a) indicates a decrease of
458 about 4 °C at the near-surface over the dried Dead Sea area in contrast to negligible
459 changes on a parallel transect inland, on the western coast of the Dead Sea. These
460 evidences the notorious impact of the absence of water in the valley temperature, thus,
461 gradients in the region. The colder valley temperatures do not favour the downward
462 penetration of the MSB, which strongly affects the atmospheric conditions in the valley.
463 Moreover, a north-easterly land breeze is visible from about 20 UTC on the eastern shore
464 of the Dead Sea in the REF^{19,11} simulation, but not in the SEN^{19,11} simulation (Figure
465 10b). This situation reflects an interesting case different from the ones generally
466 presented in former investigations in the area (e.g. Alpert et al. 1997 ; and Alpert et al.
467 2006b) in which due to the recent weakening of the Dead-Sea breeze, mainly because
468 of the drying and shrinking of the Sea, the Mediterranean breeze penetrates stronger
469 and earlier into the Dead-Sea Valley increasing the evaporation because of the strong,
470 hot and dry wind.

471 Mountain downslope winds develop in both simulations from about 22 UTC. One hour
472 later, strong northerly valley flow in the northern part of the Dead Sea contrasts with the
473 westerly flow in the SEN^{19,11} simulation (Figure 10c). As the valley cools down during
474 night time in the SEN simulation, T2m decreases about 1 K from 20 UTC to 03 UTC in
475 contrast with the 0.1 K decrease of the Dead Sea in the REF simulation, the temperature
476 gradient weakens and the northerly valley flow present in the REF simulation is absent
477 in the SEN simulation. During the night, the synoptic conditions gain more influence than
478 the local wind systems governing the conditions in the valley during day time. South-
479 easterly winds prevail in the valley in both simulations. Much stronger wind velocities are



480 reached in the REF simulation, confirming the sensitivity of large-scale dynamics to near-
481 surface climate change-induced impacts.

482 The encounter of the north north-westerly and south south-easterly winds over the Dead
483 Sea area in the REF^{19,11} simulation induces the formation of a convergence zone, which
484 intensifies and extends offshore over the next hours and determines the location of
485 convective initiation. Meanwhile, homogeneous south-easterly winds are observed in the
486 SEN simulation (Figure 10d).

487 The differences in the wind circulations contribute to a different distribution of the
488 atmospheric conditions in the target area, particularly, low-tropospheric water vapour as
489 seen in the vertical cross sections in Figure 11. The evolution of the atmospheric
490 conditions in the 3-h period prior to convective initiation evidences the deeper and wetter
491 boundary layer in the REF^{19,11} simulation at the north-western foothills of the ridge at the
492 Jordanian Highlands. Differences of IWV up to 2 mm, and of instability (CAPE) close to
493 200 J/kg are found in this area (not shown). This is the location of the convergence line
494 where convective updrafts, which start close to the ground, are triggered reaching a
495 maximum vertical velocity of about 5 m/s above the convergence zone in the REF^{19,11}
496 simulation.

497

498 **4. Conclusions**

499 The drying and shrinking of the Dead Sea has been extensively investigated in the last
500 decades from different points of view. This process has been related to significant local
501 climate changes which affect the Dead Sea valley and neighboring regions. The climate
502 of the Dead Sea is very hot and dry. But occasionally the Dead Sea basin is affected by
503 severe convection generating heavy precipitation, which could lead to devastating flash
504 floods.

505 In this study, high-resolution COSMO model simulations are used to assess the impact
506 of the Dead Sea on the occurrence of convective precipitation in the region. A set of high-
507 resolution, ~ 2.8 km, climate simulations covering the period 2003 to 2013, and several
508 numerical weather prediction (NWP) runs on an event time scale (~ 48-36 h) are
509 performed over the Dead Sea area. On a decadal time scale, two simulations are carried
510 out. The first “reference” run with the Dead Sea area, and a second run “sensitivity” in
511 which the Dead Sea is dried out and set to bare soil. The NWP simulations focus on two
512 heavy precipitation events exhibiting relevant differences between the reference and the
513 sensitivity decadal runs. A total of four simulations are performed in this case.



514 As the energy balance partitioning of the Earth's surface changes due to the drying of
515 the Dead Sea, relevant impacts could be identified in the region. From a climatological
516 point of view, in a future regional climate under ongoing Dead Sea level decline, less
517 evaporation, higher air temperatures and less precipitation is to expect. Reduced
518 evaporation over the Dead Sea occurs from May to October. The cooling effect of
519 evaporation in the neighboring areas results in an increase of T-2m in the absence of
520 the Dead Sea. Atmospheric conditions, such as air temperature and humidity, are mostly
521 affected in the lower-tropospheric levels, which in turn influence atmospheric stability
522 conditions, hence, precipitating convection. The number of dry days is reduced, but in
523 general the number of dry/wet days is not largely affected by the drying of the Dead Sea;
524 rather the structure and intensity of the heavier precipitation events is changed. While a
525 general and homogeneous decrease in evaporation is seen at the SEN^{CLIM} simulation,
526 precipitation deviations occur in both directions, which could suggest and impact on the
527 timing of the events. A relevant year to year variability is observed in evaporation-
528 precipitation which indicates the need of long time series of observations to understand
529 local conditions and to validate model simulations.

530 The detailed analysis of two heavy precipitation events allowed us to further assess the
531 possible causes and the processes involved regarding the decrease in precipitation
532 intensity or the total omission of convection with respect to the reference simulation in
533 the absence of the Dead Sea water. Two main components, strongly affected by the
534 drying of the Dead Sea, are found to be highly relevant for the understanding of the
535 environmental processes in the Dead Sea region.

536 (a) First, the lower-atmospheric boundary layer conditions. Changes in the energy
537 balance affect the atmosphere through the heat exchange and moisture supply. The
538 drying of the Dead Sea in the SEN simulations and the resulting decrease in local
539 evaporation, impact the Dead Sea Basin conditions and the neighbouring areas. A
540 reduction in boundary layer humidity and an increase in temperature result in a general
541 decrease of atmospheric instability and weaker updrafts indicating reduced deep-
542 convective activity. Main differences on the atmospheric conditions are directly over the
543 Dead Sea, but these conditions are frequently advected to neighbouring areas by the
544 thermally driven wind systems in the region which play a key role for the redistribution of
545 these conditions and the initiation of convection.

546 (b) Secondly, wind systems in the valley. In the arid region of the Dead Sea Basin with
547 varied topography, thermally and dynamically driven wind systems are key features of
548 the local climate. Three different scales of climatic phenomena coexist: The



549 Mediterranean Sea Breeze (MSB), the Dead Sea breeze and the orographic winds,
550 valley-, and slope-winds, which are known to temper the climate in the Dead Sea valley
551 (Shafir and Alpert, 2011). The drying of the Dead Sea in the SEN simulation disturbs the
552 Dead Sea thermally driven wind circulations. The Dead Sea breezes are missing, weaker
553 wind speeds characterize the region and along valley winds are consequently affected.
554 Furthermore, the dynamics of the Mediterranean breeze penetration into the Jordan
555 Valley are affected.

556

557 Consequently, the impacts on convection initiation and development are twofold:

558 (i) Distinct redistribution of atmospheric conditions, locally or remotely, which yields to
559 different atmospheric conditions that in the absence of the Dead Sea result in a reduced
560 moisture availability in the lower atmospheric levels and increased stability hindering
561 convection or reducing the intensity of the events.

562 (ii) Modification of the divergence/convergence field. The absence of the Dead Sea
563 substantially modifies the wind circulation systems over the Dead Sea valley, which leads
564 to the omission of convergence lines which act as triggering mechanism for convection.

565

566 We can conclude that in general the lack of sufficient low-atmospheric moisture in
567 relation to the drying of the Dead Sea, the increase of atmospheric stability in addition to
568 an absence or reduction in the intensity of the convergence zones, works against
569 initiation or intensification of precipitating convection in the area. The relevance of the
570 small-scale variability of moisture and the correct definition and location of convergence
571 lines for an accurate representation of convective initiation illustrates the limitation and
572 the lack of adequate observational networks in the area and the need for high-resolution
573 model simulations of boundary layer processes to predict intense and localised
574 convection in the region.

575 These results contribute to gain a better understanding of expected conditions in the
576 Dead Sea valley and neighbouring areas under continual lake level decline. Energy
577 balance partitioning and wind circulation systems are determinant for local climatic
578 conditions, e.g. temperature and humidity fields as well as aerosol redistribution,
579 therefore, any change should be well understood and properly represented in model
580 simulations of the region. In a further step, the authors will assess the impact of model
581 grid resolution on the horizontal and vertical flow field in the region across scales,
582 including the impact on large-scale dynamics. We will also put emphasis in trying to
583 better understand the dynamics of the MSB under lake level decline using high-resolution
584 modelling, especially the contrasting behaviour pointed out in this study. Fine resolution



585 simulations up to 100 m will be performed for this purpose. Furthermore, we will provide
586 a verification of the complex chain of processes in the area using unique measurements
587 in the framework of the interdisciplinary virtual institute Dead Sea Research VEnue
588 (DESERVE; Kottmeier et al., 2016).

589

590 **Author contribution**

591 SK wrote the manuscript, analysed the data, interpreted the results and supervised the
592 work. JH carried out data analysis, interpretation of results and prepared all the figures.

593

594 **Acknowledgements**

595 The first author's research was supported by the Bundesministerium für Bildung und
596 Forschung (BMBF; German Federal Ministry of Education and Research). The authors
597 acknowledge the colleagues at the Karlsruhe Institute of Technology (KIT) involved in
598 the interdisciplinary virtual institute Dead Sea Research VEnue (DESERVE) for their
599 support and interesting discussions. We acknowledge Sebastian Helgert and Alberto
600 Caldas Alvarez for their assistance in the preparation of the simulations. This article is a
601 contribution to the HyMeX program.

602

603

604

605

606

607

608

609

610

611



612 **References**

- 613 Alpert, P., and Shay-EL, Y.: The Moisture Source for the Winter Cyclones in the Eastern
614 Mediterranean. *Israel Meteorological Research Papers*, 5, 20-27, 1994.
- 615 Alpert, P., and Coauthors: Relations between climate variability in the Mediterranean
616 region and the tropics: ENSO, South Asian and African monsoons, hurricanes
617 and Saharan dust. *Developments in Earth and Environmental Sciences*, 4, 149-
618 177, [https://doi.org/10.1016/S1571-9197\(06\)80005-4](https://doi.org/10.1016/S1571-9197(06)80005-4), 2006.
- 619 Alpert, P., Shafir, H., and Issahary, D.: Recent Changes in the Climate At the Dead Sea
620 – a Preliminary Study. *Climatic Change*, 37(3), 513-537,
621 <https://doi.org/10.1023/A:1005330908974>, 1997.
- 622 Andersson, T., Andersson, M., Jacobsson, C., Nilsson, S.: Thermodynamic
623 indices for forecasting thunderstorms in southern Sweden. *Meteorol. Mag.*
624 116, 141-146, 1989.
- 625 Arkin, Y., and Gilat, A.: Dead Sea sinkholes - an ever-developing hazard. *Environmental*
626 *Geology*, 39(7), 711-722, <https://doi.org/10.1007/s002540050485>, 2000.
- 627 Ashbel, D., and Brooks, C.: The influence of the dead sea on the climate of its
628 neighbourhood. *Quarterly Journal of the Royal Meteorological Society*, 65(280),
629 185-194, <https://doi.org/10.1002/qj.49706528005>, 1939.
- 630 Ban, N., Schmidli, J., and Schär, C.: Evaluation of the convection-resolving
631 regional climate modeling approach in decade-long simulations, *J. Geophys.*
632 *Res. Atmos.*, 119, 7889– 7907, <https://doi.org/10.1002/2014JD021478>, 2014.
- 633 Belachsen, I., Marra, F., Peleg, N., and Morin, E.: Convective rainfall in dry climate:
634 relations with synoptic systems and flash-flood generation in the Dead Sea
635 region. *Hydrology and Earth System Sciences Discussions*, 21, 5165-5180,
636 <https://doi.org/10.5194/hess-21-5165-2017>, 2017.
- 637 Böhm, U., and Coauthors: The Climate Version of LM: Brief Description and Long-Term
638 Applications. *COSMO Newsletter*, 6, 225-235, 2006.
- 639 Businger, J., Wyngaard, J., Izumi, Y., and Bradley, E.: Flux-Profile Relationships in the
640 Atmospheric Surface Layer. *Journal of the Atmospheric Sciences*, 28(2), 181-
641 189, [https://doi.org/10.1175/1520-0469\(1971\)028<0181:FPRITA>2.0.CO;2](https://doi.org/10.1175/1520-0469(1971)028<0181:FPRITA>2.0.CO;2),
642 1971.



- 643 Byun, H., and Kim, D.: Comparing the Effective Drought Index and the Standardized
644 Precipitation Index. *Options Méditerranéennes. Séries A. Mediterranean*
645 *Seminars*, 95, 85-89, 2010.
- 646 Byun, H., and Wilhite, D.: Objective quantification of drought severity and duration. *J.*
647 *Climate*, 12(9), 2747-2756, [https://doi.org/10.1175/1520-](https://doi.org/10.1175/1520-0442(1999)012<2747:OQODSA>2.0.CO;2)
648 [0442\(1999\)012<2747:OQODSA>2.0.CO;2](https://doi.org/10.1175/1520-0442(1999)012<2747:OQODSA>2.0.CO;2), 1999.
- 649 Cohen, S., and Stanhill, G.: Contemporary Climate Change in the Jordan Valley. *J. Appl.*
650 *Meteor.*, 35(7), 1051-1058, [https://doi.org/10.1175/1520-](https://doi.org/10.1175/1520-0450(1996)035<1051:CCCITJ>2.0.CO;2)
651 [0450\(1996\)035<1051:CCCITJ>2.0.CO;2](https://doi.org/10.1175/1520-0450(1996)035<1051:CCCITJ>2.0.CO;2), 1996.
- 652 Corsmeier, U., Behrendt, R., Drobinski, P., Kottmeier, C.: The mistral and its
653 effect on air pollution transport and vertical mixing, *Atmos. Res.*, 74, 275–302,
654 <https://doi.org/https://doi.org/10.1016/j.atmosres.2004.04.010>, 2005.
- 655 Dayan, U., and Morin, E.: Flash flood – producing rainstorms over the Dead Sea: A
656 review. *Geological Society of America*, 401(4), 53-62,
657 [https://doi.org/10.1130/2006.2401\(04\)](https://doi.org/10.1130/2006.2401(04)) , 2006.
- 658 Dayan, U., and Sharon, D.: Meteorological parameters for discriminating between
659 widespread and spotty storms in the Negev. *Israel Journal of Earth Sciences*,
660 29(4), 253-256, 1980.
- 661 Dayan, U., Ziv, B., Margalit, A., Morin, E., and Sharon, D.: A severe autumn storm over
662 the middle-east: synoptic and mesoscale convection analysis. *Theoretical and*
663 *Applied Climatology*, 69(1-2), 103-122, <https://doi.org/10.1007/s007040170038>,
664 2001.
- 665 Doms, G., and Baldauf, M.: A Description of the Nonhydrostatic Regional COSMO-
666 Model. Part I: Dynamics and Numerics. Deutscher Wetterdienst, 2015.
- 667 Doms, G., and Coauthors: A Description of the Nonhydrostatic Regional COSMO Model
668 Part II : Physical Parameterization. Deutscher Wetterdienst, 2011.
- 669 Doswell, C., and Rasmussen, E.: The Effect of Neglecting the Virtual Temperature
670 Correction on CAPE Calculations. *Weather and Forecasting*, 9(4), 625-629,
671 [https://doi.org/10.1175/1520-0434\(1994\)009<0625:TEONTV>2.0.CO;2](https://doi.org/10.1175/1520-0434(1994)009<0625:TEONTV>2.0.CO;2), 1994.
- 672 FAO/IIASA/ISRIC/ISSCAS/JRC.: Harmonized World Soil Database (version 1.2). FAO,
673 Rome, Italy and IIASA, Laxenburg, Austria, (accessed 01.02.2017) , 2009.
- 674 Fossier, G., Khodayar, S., and Berg, P.: Benefit of convection permitting climate



- 675 model simulations in the representation of convective precipitation, *Clim. Dyn.*,
676 44(1–2), 45–60.
- 677 Gavrieli, I., Bein, A., and Oren, A., 2005: The expected impact of the “Peace Conduit”
678 project (the Red Sea - Dead Sea pipeline) on the Dead Sea. *Mitigation and*
679 *Adaptation Strategies for Global Change*, 10(4), 759-777,
680 <https://doi.org/10.1007/s11027-005-5144-z>.
- 681 European Commission, Joint Research Centre, 2003: Global Land Cover 2000
682 database, (accessed 01.02.2017).
- 683 GLOBE National Geophysical Data Center, 1999: Global Land One-kilometer Base
684 Elevation (GLOBE) v.1. Hastings, D. and P.K. Dunbar. National Geophysical
685 Data Center, NOAA, (accessed 01.02.2017).
- 686 Greenbaum, N., Ben-Zvi, A., Haviv, I., and Enzel, Y., 2006: The hydrology and
687 paleohydrology of the Dead Sea tributaries. *Geological Society of America*,
688 401(4), 63-93, [https://doi.org/10.1130/2006.2401\(05\)](https://doi.org/10.1130/2006.2401(05)).
- 689 Houze, R., 2012: Orographic effects on precipitating clouds. *Reviews of Geophysics*,
690 50(1), <https://doi.org/10.1029/2011RG000365>.
- 691 Kalthoff, N., Horiacher, V., Corsmeier, U., Volz-Thomas, A., Kolahgar, B., Geiß, H.,
692 Möllmann-Coers, M., and Knaps, A. 2000: Influence of valley winds on transport
693 and dispersion of airborne pollutants in the Freiburg-Schauinsland area, *J.*
694 *Geophys. Res. Atmos*, 105, 1585–1597, <https://doi.org/10.1029/1999jd900999>.
- 695
696 Khodayar, S., Kalthoff, N., and Schaedler, G., 2013: The impact of soil moisture
697 variability on seasonal convective precipitation simulations. Part I: validation,
698 feedbacks, and realistic initialisation. *Meteorologische Zeitschrift*, 22(4), 489-505,
699 <https://doi.org/10.1127/0941-2948/2013/0403>.
- 700 Llasat, M., and Coauthors, 2010: High-impact floods and flash floods in Mediterranean
701 countries: the FLASH preliminary database. *Advances in Geosciences*, 23, 47-
702 55, <https://doi.org/10.5194/adgeo-23-47-2010>.
- 703 Metzger, J., Nied, M., Corsmeier, U., Kleffmann, J., and Kottmeier, C., 2017: Dead Sea
704 evaporation by eddy covariance measurements versus aerodynamic, energy
705 budget, Priestley-Taylor, and Penman estimates. *Hydrology and Earth System*
706 *Sciences Discussions*, 22(2), 1135-1155, <https://doi.org/10.5194/hess-2017-187>.



- 707 Moncrieff, M., and Miller, M., 1976: The dynamics and simulation of tropical
708 cumulonimbus and squall lines. *Quarterly Journal of the Royal Meteorological*
709 *Society*, 102(432), 373-394, <https://doi.org/10.1002/qj.49710243208>, 2014.
- 710 Naor, R., Potchter, O., Shafir, H., and Alpert, P.: An observational study of the
711 summer Mediterranean Sea breeze front penetration into the complex
712 topography of the Jordan Rift Valley, *Theor. Appl. Climatol.*, 127, 275–284,
713 <https://doi.org/10.1007/s00704-015-1635-3>, 2017.
- 714 Prein, A., Gobiet, A., Suklitsch, M., Truhetz, H., Awan, N., Keuler, K., and Georgievski,
715 G. : Added value of convection permitting seasonal simulations, *Clim.*
716 *Dyn.*, 41(9– 10), 2655– 2677, 2013.
- 717 Schaedler, G., and Sasse, R.: Analysis of the connection between precipitation and
718 synoptic scale processes in the Eastern Mediterranean using self-organizing
719 maps. *Meteorologische Zeitschrift*, 15(3), 273-278, [https://doi.org/10.1127/0941-](https://doi.org/10.1127/0941-2948/2006/0105)
720 [2948/2006/0105](https://doi.org/10.1127/0941-2948/2006/0105), 2006.
- 721 Shafir, H., and Alpert, P.: Regional and local climatic effects on the Dead-Sea
722 evaporation. *Climatic Change*, 105(3-4), 455-468,
723 <https://doi.org/10.1007/s10584-010-9892-8>, 2011.
- 724 Sharon, D., and Kutiel, H.: The distribution of rainfall intensity in Israel, its regional and
725 seasonal variations and its climatological evaluation. *International Journal of*
726 *Climatology*, 6(3), 277-291, <https://doi.org/10.1002/joc.3370060304>, 1986.
- 727 Smiatek, G., Kunstmann, H., and Heckl, A.: High-resolution climate change simulations
728 for the Jordan River area. *Journal of Geophysical Research*, 116(D16),
729 <https://doi.org/10.1029/2010JD015313>, 2011.
- 730 Stanhill, G.: Changes in the rate of evaporation from the dead sea. *International Journal*
731 *of Climatology*, 14(4), 465-471, <https://doi.org/10.1002/joc.3370140409>, 1994.
- 732 Vicente-Serrano, S., Beguería, S., López-Moreno, J.: A Multiscalar Drought Index
733 Sensitive to Global Warming: The Standardized Precipitation Evapotranspiration
734 Index. *J. Climate*, 23(7), 1696-1718, <https://doi.org/10.1175/2009JCLI2909.1>,
735 2010.
- 736 Vüllers, J., Mayr, G. J., Corsmeier, U., and Kottmeier, C.: Characteristics and
737 evolution of diurnal foehn events in the Dead Sea valley. *Atmos. Chem. Phys.*,
738 18, 18169-18186, <https://doi.org/10.5194/acp-18-18169-2018>, 20, 2018.



739 Wernli H, Paulat M, Hagen M, Frei C. SAL – a novel quality measure for the
740 verification of quantitative precipitation forecasts. *Mon. Weather Rev.* 136: 4470–
741 4487, 2008.

742

743

744

745

746

747

748

749

750

751

752

753

754

755

756

757

758

759

760

761

762

763



764 **Tables**

	PREC diffmn	REF PMX	SEN PMX	Synoptic Situation	REF CAPEmx	SEN CAPEmx	REF KOMn	SEN KOMn	Localised/ Widespread (Subarea affected)
09.12.2004	-0,10	30,09	31,31	ARST	1	1	4,85	4,85	W (A1, A2)
14.01.2006	0,11	45,64	54,64	Cyprus Low	239	225	6,57	6,54	L/W (A1, A3)
17.04.2006	-0,11	57,41	56,09	Syrian Low	43	47	1,97	1,94	L (A1, A4)
11.04.2007	-0,29	42,61	70,20	Cyprus Low	686	679	-4,77	-4,70	L (A2, A4)
14.04.2007	-0,12	134,36	127,79	Cyprus Low	573	576	-1,95	-1,92	L (A1, A2, A3, A4)
13.05.2007	0,16	41,82	47,90	Syrian Low	436	81	-5,30	-5,29	L (A1, A2)
28.01.2008	0,14	23,11	17,24	Syrian Low	7	7	5,12	5,12	W (A1, A3)
26.10.2008	0,23	139,01	125,73	ARST	1274	1361	-5,50	-4,08	L (A3)
14.11.2008	-0,30	40,83	45,55	ARST	25	7	1,37	1,38	L (A2, A4)
15.05.2009	0,39	59,28	68,84	Syrian Low	433	429	-3,90	-3,91	L (A1, A2, A3, A4)
16.05.2009	-0,20	49,23	42,28	Syrian Low	208	203	-2,30	-2,36	L (A1, A2, A3)
01.11.2009	0,19	166,21	111,79	Cyprus Low	435	445	-5,03	-4,46	L (A1, A2)
16.01.2011	-0,11	73,02	72,03	Syrian Low	49	37	7,82	7,83	L/W (A1, A4)
29.05.2011	0,24	44,51	32,73	Cyprus Low	158	170	-10,27	-10,26	W (A2)
16.11.2011	0,11	42,65	9,34	Cyprus Low	2	0	-7,14	-7,12	L (A1, A2)
18.11.2011	-0,11	90,07	93,04	Cyprus Low	386	304	-9,14	-9,16	L (A1)
19.11.2011	0,11	28,68	34,69	Cyprus Low	356	378	-8,61	-8,65	L (A1)
20.11.2011	-0,03	58,11	12,36	Cyprus Low	133	81	-7,60	-7,46	L (A2, A4)
23.10.2012	-0,20	29,88	41,64	ARST	2068	2097	-5,83	-5,59	L (A1, A2)
10.11.2012	0,11	27,20	22,56	Cyprus Low	218	215	3,97	3,98	W (A1)
24.11.2012	0,21	155,77	117,81	ARST	189	286	-2,18	-1,95	L (A1, A2, A3)
26.11.2012	0,11	41,48	54,33	ARST	354	332	4,19	4,37	L (A3, A4)

765

766

767 **Table 1:** Classification of heavy precipitation cases in the decadal simulation covering
 768 the period 2004 to 2013. The areal-mean (study area, Figure 1) difference (PREC_{diffmn})
 769 and maximum grid precipitation in the reference (REF_{PMX}) and sensitivity (SEN_{PMX})
 770 realizations, the synoptic situation, and the stability conditions illustrated by maximum
 771 grid point CAPE (CAPE_{mx}) and minimum grid point KO-index (KOMn) are summarized.
 772 Additionally, the nature of the precipitation, localized (L) or widespread (W) and the main
 773 subarea affected (following division in Figure 1; A1, A2, A3, A4) are listed.

774

775

776

777

778

779

780

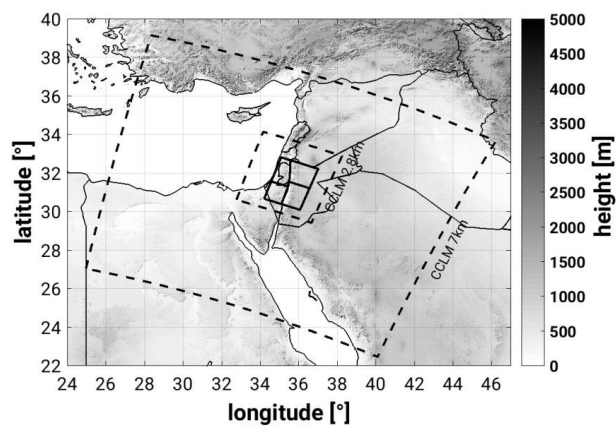
781



782

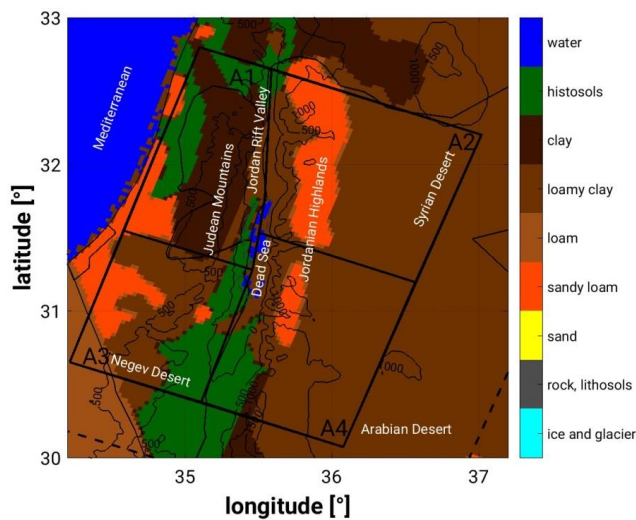
783 **Figures**

784 (a)



785

786 (b)



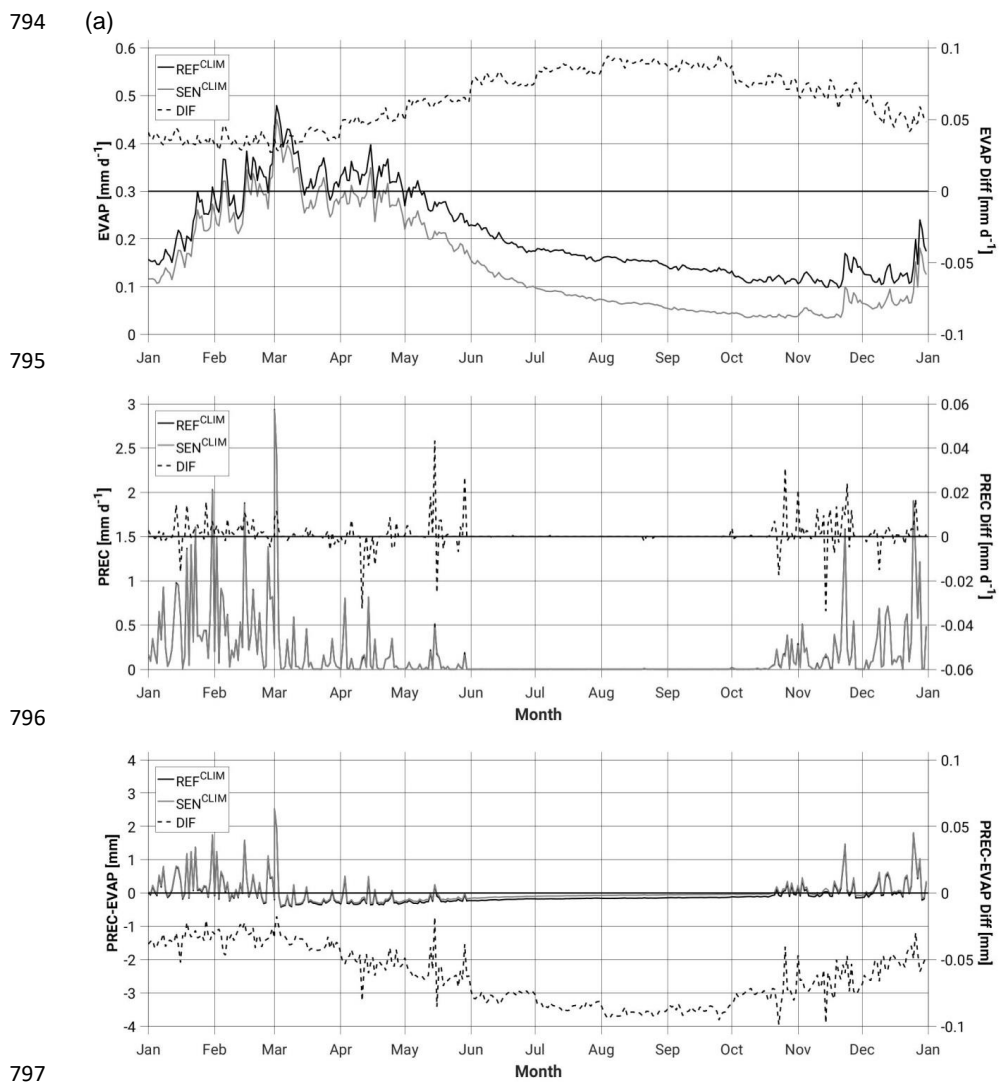
787

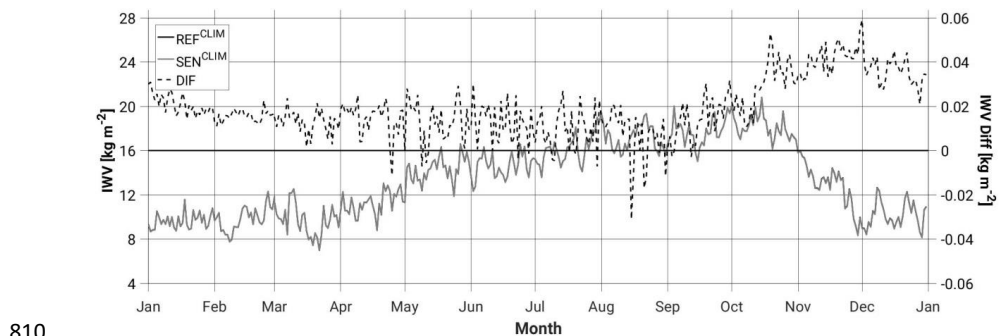
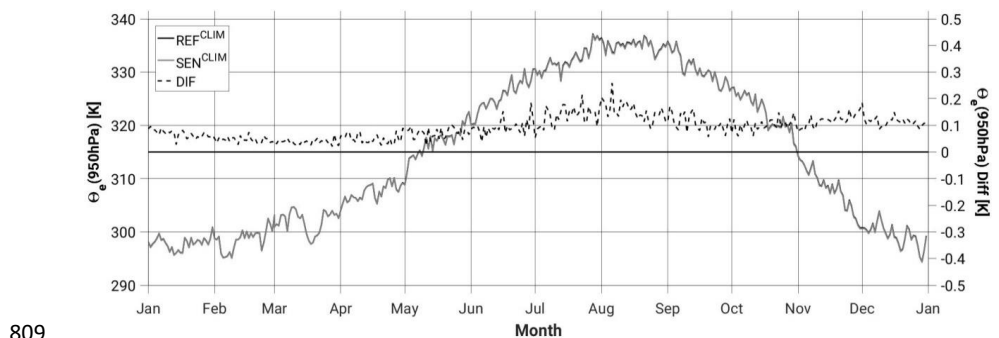
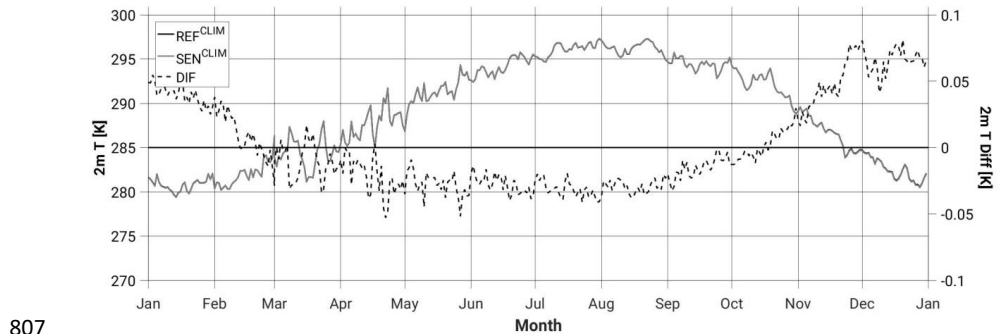
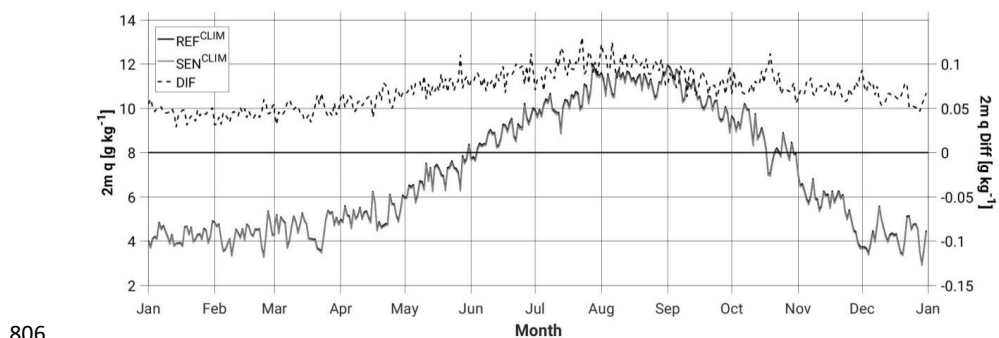
788

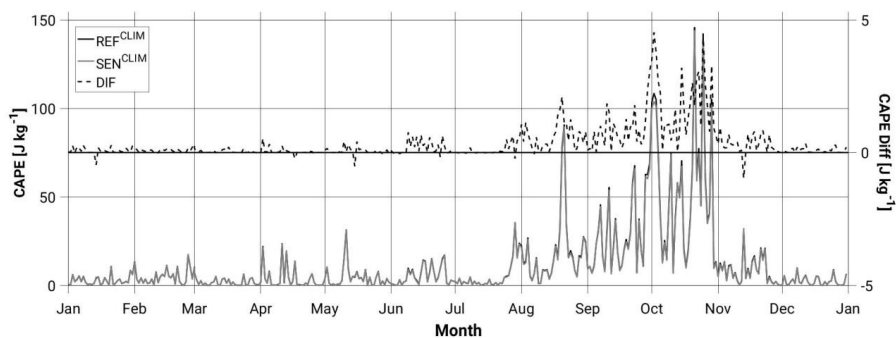
789 Figure 1: (a) Topography (m above msl), simulation domains (dashed lines) and study
790 area (bold line). (b) Model soil types (colour scale), topography (black isolines) and study
791 area (black bold line) including the 4 subdomains to be examined, A1-4 (Area 1-4).

792

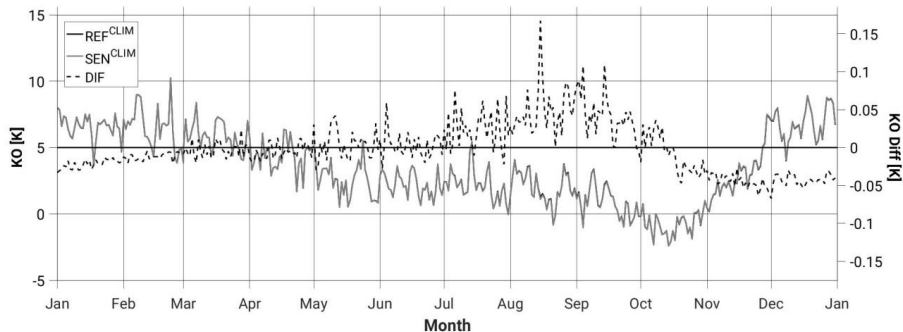
793







812



813

814

815

816 Figure 2: Annual cycle of the areal-daily averaged (and differences (black dashed line))
817 of (a) evaporation, precipitation, and precipitation minus evaporation (b) specific humidity
818 and temperature at 2-m, and (c) Θ_e below 950 hPa and IWV, and (d) CAPE and KO-
819 index, from the REF^{CLIM} (full black line) and the SEN^{CLIM} (full grey line) simulations. All
820 grid points in the investigation domain (Figure 1) and the period 2004 to 2013 are
821 considered.

822

823

824

825

826

827

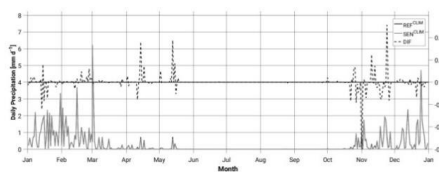
828

829

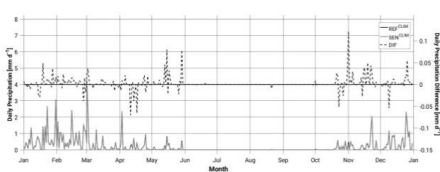
830 (a)



831 Area1 (NW)

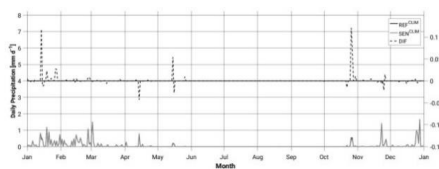


Area2 (NE)

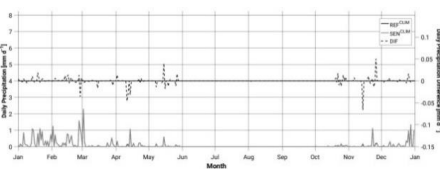


832

833 Area3 (SW)



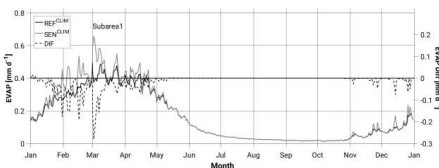
Area4 (SE)



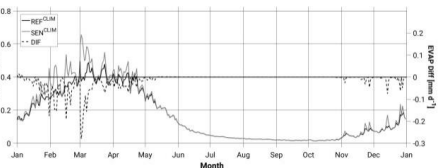
834

835 (b)

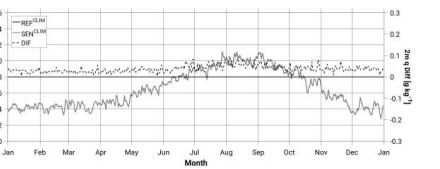
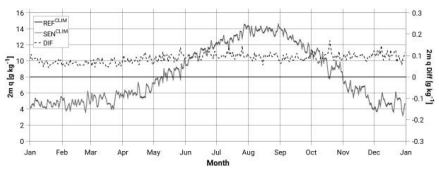
836 Area1 (NW)



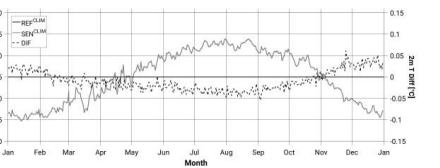
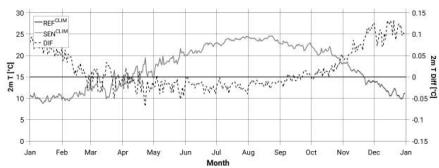
Area2 (NE)



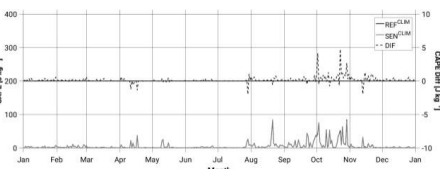
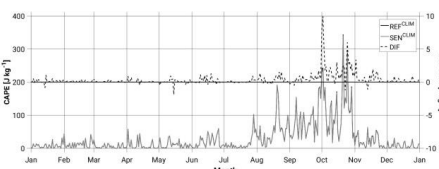
837



838



839



840

841

842



843 Figure 3: Annual cycle of the areal-daily averaged (and differences (black dashed line))
844 of (a) precipitation for areas A1, A2, A3, A4 (see Figure 1b), and (b) evaporation, specific
845 humidity and temperature at 2-m, and CAPE for areas A1 and A2, from the REF^{CLIM} (full
846 black line) and the SEN^{CLIM} (full grey line) simulations. Only land points in the
847 investigation domain (Figure 1) and the period 2004 to 2013 are considered.

848

849

850

851

852

853

854

855

856

857

858

859

860

861

862

863

864

865

866

867

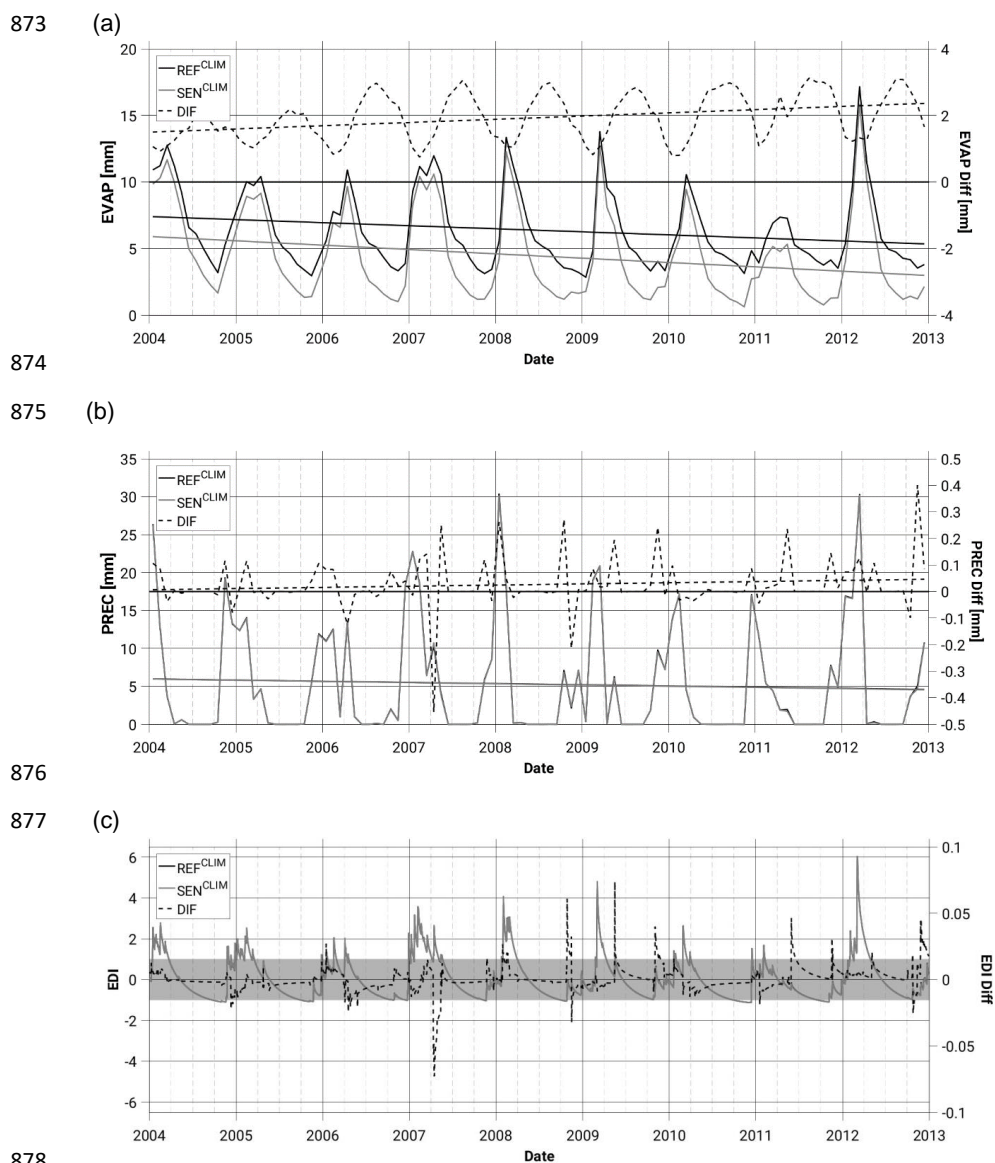
868

869

870

871

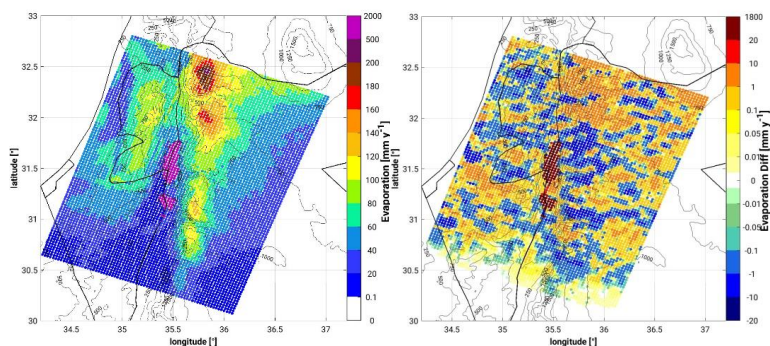
872



880 Figure 4: Temporal evolution of the monthly-daily areal mean values of (a) Evaporation,
881 (b) Precipitation, (c) Effective Drought Index (EDI), from the REF^{CLIM} (full black line) and
882 the SEN^{CLIM} (full grey line) simulations. Differences are depicted with black dashed lines.
883 The light grey band in (c) indicates the common soil state ($-1 < EDI < +1$). All grid points in
884 the investigation domain (Figure 1) and the period 2004 to 2013 are considered.

885

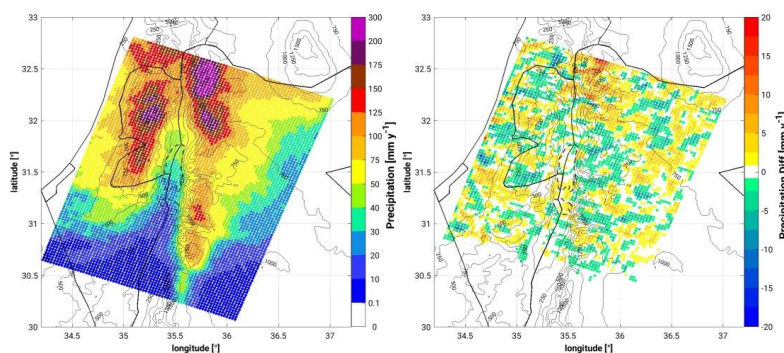
886 (a)



887

888

889 (b)



890

891

892 Figure 5: Spatial distribution of (a) evaporation in the REF^{CLIM} simulation (left) and the
893 difference between the REF^{CLIM} and SEN^{CLIM} simulations (right), and (b) precipitation in
894 the REF^{CLIM} simulation (left) and the difference between the REF^{CLIM} and SEN^{CLIM}
895 simulations (right). The period 2004 to 2013 is considered.

896

897

898

899

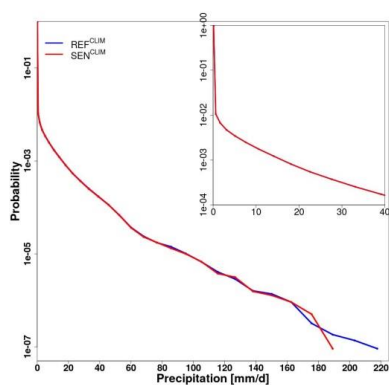
900

901

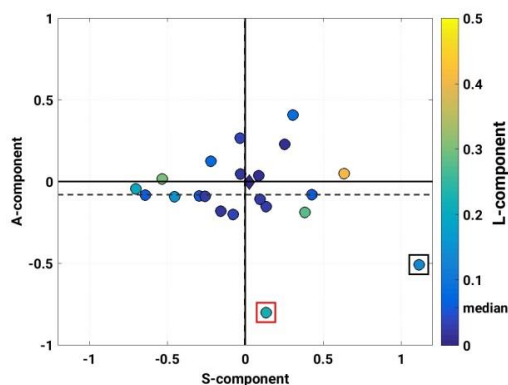
902



903 (a)



(b)



904

905

906

907 Figure 6: (a) Probability density function of daily precipitation intensities. All grid points
908 in the investigation domain (Figure 1) and the period 2004 to 2013 are considered. (b)
909 SAL diagram between REF^{CLIM} and SEN^{CLIM} simulations. Every circle corresponds to a
910 simulated heavy precipitation event (listed in Table 1). The diamond (close to the zero-
911 zero) illustrates the mean of all events. A-component (amplitude), S-component
912 (structure), L-component (location). The inner colour indicates the L-component.
913 Squares point out the two events examined in this study, CASE1 and CASE2 (see
914 section 3.2).

915

916

917

918

919

920

921

922

923

924

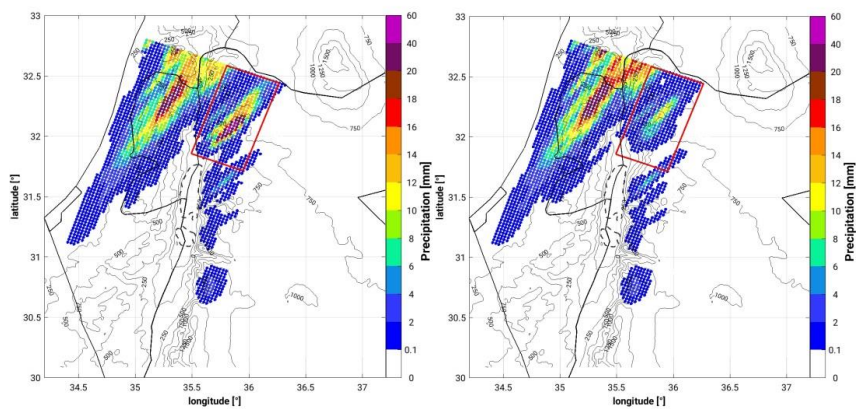
925

926



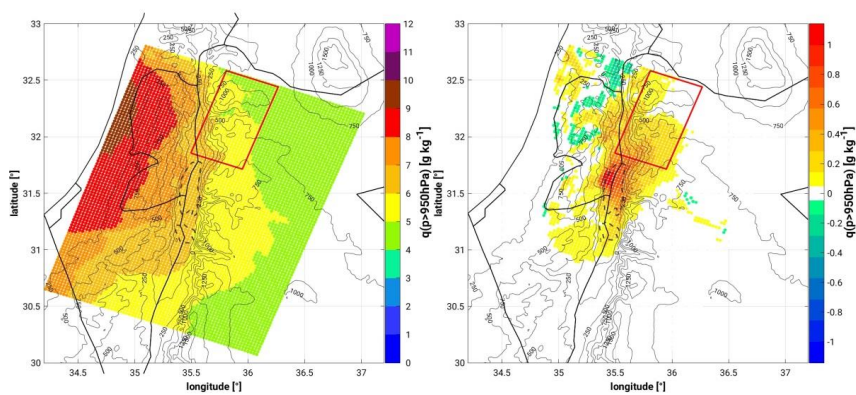
927

928 (a)



929

930 (b)



931

932

933

934

935

936

937

938

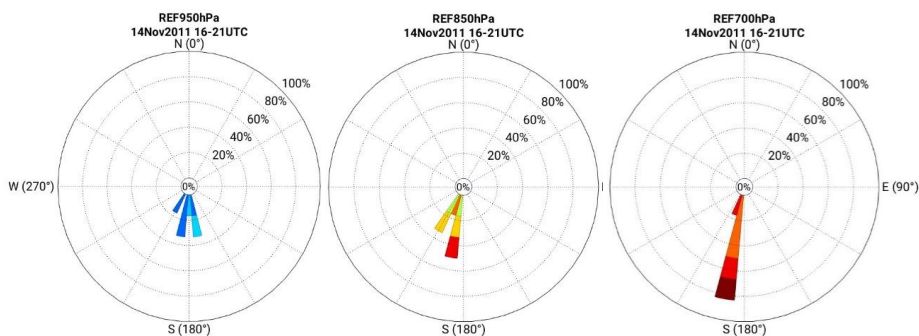
939

940

941

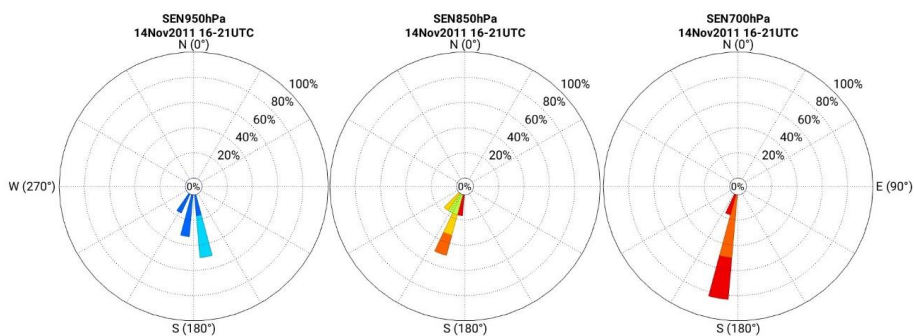


942 (c)



943

944



945



946

947

948

949

950



951 Figure 7: Spatial distribution of 24-h mean from 14.11 09 UTC to 15.11 08 UTC of, (a)
952 precipitation and (b) specific humidity below 950 hPa, from the REF^{14.11} simulation (left)
953 and the difference between the REF^{14.11} and SEN^{14.11} simulations, as a mean for the 6-h
954 period prior to convection initiation in the target area (14 November 16 UTC to 21 UTC),
955 and (c) wind conditions at 700 hPa, 850 hPa, and 950 hPa (no relevant differences with
956 respect to the 10-m field) for the same time period. Wind roses are centred at about
957 35.82°E-32.07°N in our target area.

958

959

960

961

962

963

964

965

966

967

968

969

970

971

972

973

974

975

976

977

978

979

980

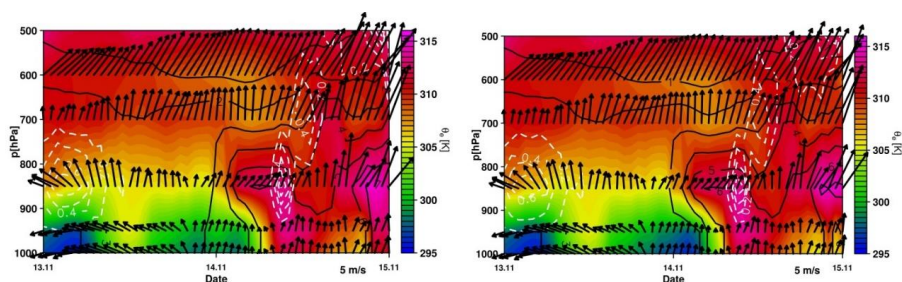
981



982

983

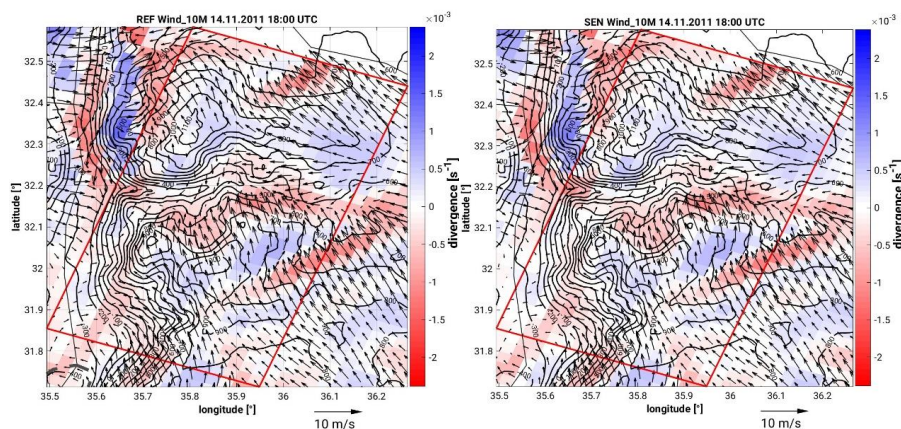
984 (a)



985

986 (b)

987



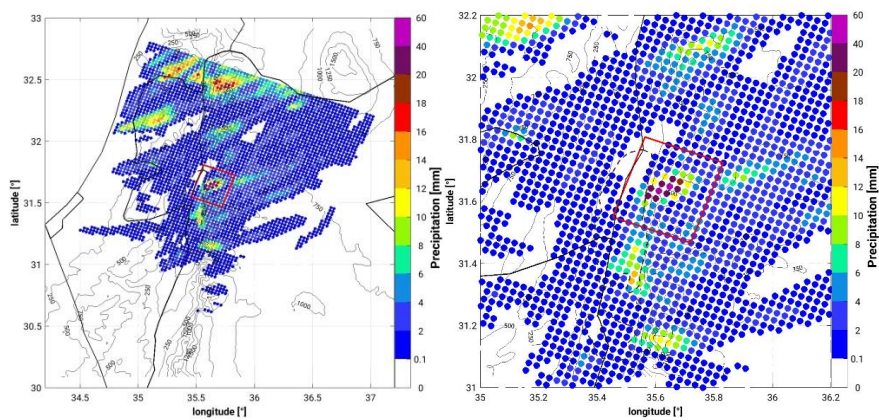
988

989

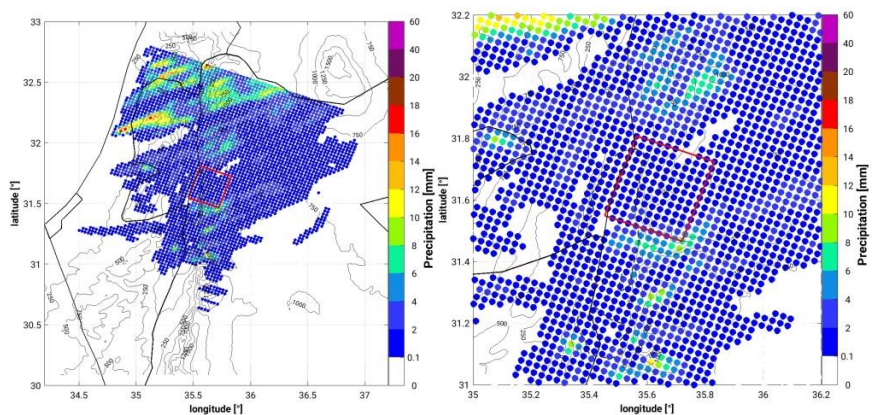
990 Figure 8: (a) Vertical-temporal cross-section of equivalent potential temperature (colour
991 scale; K), specific humidity (black isolines; g/kg), horizontal wind vectors (north-pointing
992 upwards, m/s) and vertical velocity (white dashed contours with 0.1 m/s increments) of
993 the REF^{14.11} (left) and SEN^{14.11} (right) simulations, over a representative grid point in the
994 sub-study region, 32.05°N 35.79°E. (b) Spatial distribution of 10-m horizontal wind (wind
995 vectors; m/s) and corresponding divergence/convergence field (colour scale; s⁻¹) at 18
996 UTC on the 14 November 2011 from the REF^{14.11} (left) and SEN^{14.11} (right) simulations.

997

998



999



1000
1001
1002

1003 Figure 9: 24-h mean spatial distribution of precipitation from the REF^{19,11} simulation (top-
1004 left; zoom top-right) and the SEN^{14,11} simulation (bottom-left; zoom bottom-right) for the
1005 period 18 November 2011 11 UTC to 19 November 2011 10 UTC.

1006

1007

1008

1009

1010

1011

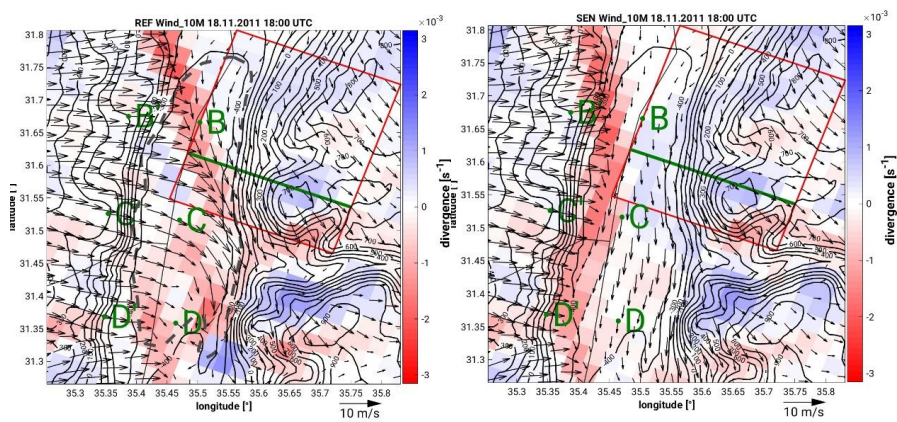
1012

1013



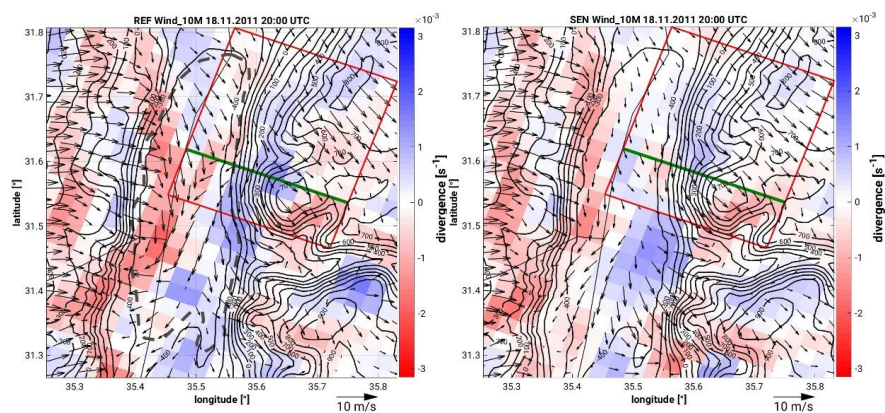
1014

1015 (a)



1016

1017 (b)



1018

1019

1020

1021

1022

1023

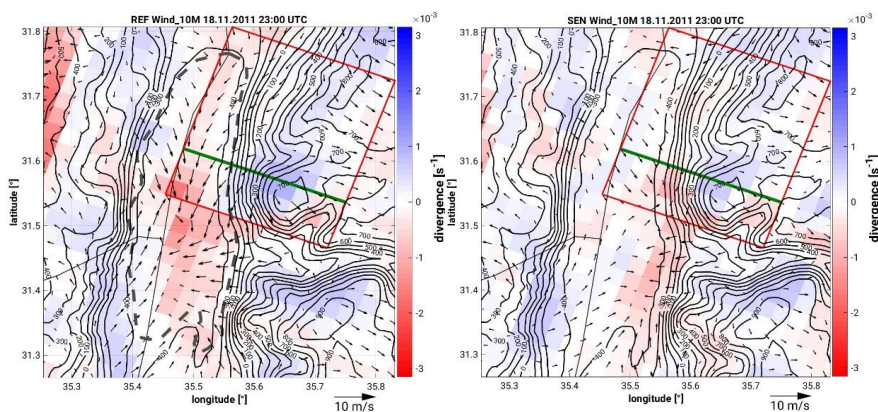
1024

1025

1026



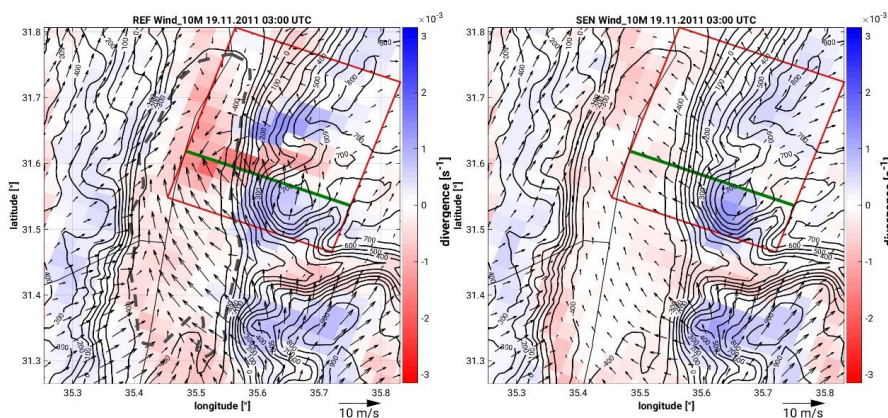
1027 (c)



1028

1029

1030 (d)



1031

1032

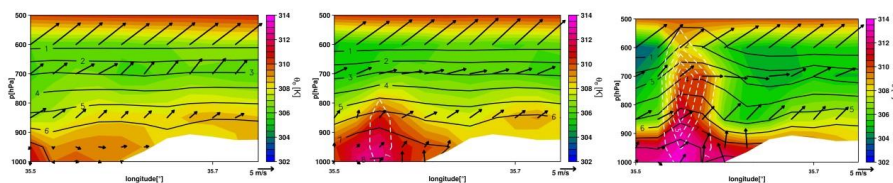
1033 Figure 10: Spatial distribution of 10-m horizontal wind (wind vectors; m/s) and
1034 corresponding divergence/convergence field (colour scale; s^{-1}) at 18 UTC, 20 UTC, 23
1035 UTC on the 19 November, and 03 UTC on the 20 November 2011 from the REF^{14,11} (left)
1036 and SEN^{14,11} (right) simulations. The topography is indicated by the black full isolines.
1037 The transects (B-C-D and B'-C'-D') corresponding to the locations in which temperature
1038 comparisons are made are indicated in Figure 10a. The green line indicates the position
1039 of the vertical cross-section in Figure 11.

1040

1041

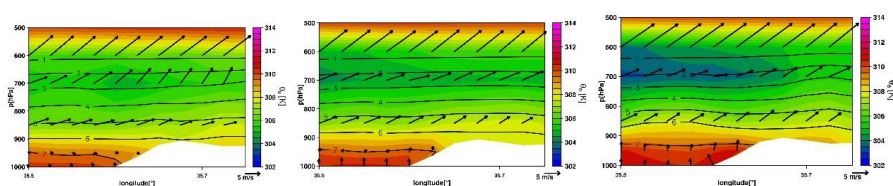


1042



1043

1044



1045

1046

1047

1048 Figure 11: Vertical cross-section of equivalent potential temperature (colour scale; K),
1049 specific humidity (black isolines; g/kg), horizontal wind vectors (north-pointing upwards,
1050 m/s) and vertical velocity (white dashed contours with 1 m/s increments) of the REF^{14,11}
1051 (top) and SEN^{14,11} (bottom) simulations at 01 UTC (left), 02 UTC (middle) and 03 UTC
1052 (right). The location of the cross-section is indicated in Figure 10.

1053

1054

1055

1056

1057

1058

1059

1060

1061

1062

1063